Acta Crystallographica Section B
Structural Science
ISSN 0108-7681

Structures of copper(II) and manganese(II) di(hydrogen malonate) dihydrate; effects of intensity profile truncation and background modelling on structure models

A. T. H. Lenstra[a]* and O. N. Kataeva[b]

[a]Department of Chemistry, University of Antwerp (UIA), Universiteitsplein 1, B-2610 Wilrijk, Belgium, and [b]A. E. Arbuzov Institute of Organic and Physical Chemistry, Russian Academy of Sciences, A. E. Arbuzovstreet 8, Kazan 420088, Russia

Correspondence e-mail: lenstra@uia.ua.ac.be

Received 13 June 2000
Accepted 5 March 2001

The crystal structures of the title compounds were determined with net intensities I derived *via* the background–peak–background procedure. Least-squares optimizations reveal differences between the low-order ($0 < s < 0.7$ Å^{-1}) and high-order ($0.7 < s < 1.0$ Å^{-1}) structure models. The scale factors indicate discrepancies of up to 10% between the low-order and high-order reflection intensities. This observation is compound independent. It reflects the scan-angle-induced truncation error, because the applied scan angle $(0.8 + 2.0 \tan\theta)^\circ$ underestimates the wavelength dispersion in the monochromated X-ray beam. The observed crystal structures show pseudo-I-centred sublattices for three of its non-H atoms in the asymmetric unit. Our selection of observed intensities ($I > 3\sigma$) stresses that pseudo-symmetry. Model refinements on individual data sets with $(h + k + l) = 2n$ and $(h + k + l) = 2n + 1$ illustrate the lack of model robustness caused by that pseudo-symmetry. To obtain a better balanced data set and thus a more robust structure we decided to exploit background modelling. We described the background intensities $B(\underset{\sim}{H})$ with an 11th degree polynomial in θ. This function predicts the local background b at each position $\underset{\sim}{H}$ and defines the counting statistical distribution $P(B)$, in which b serves as average and variance. The observation R defines $P(R)$. This leads to $P(I) = P(R)/P(B)$ and thus $I = R - b$ and $\sigma^2(I) = I$ so that the error $\sigma(I)$ is background independent. Within this framework we reanalysed the structure of the copper(II) derivative. Background modelling resulted in a structure model with an improved internal consistency. At the same time the unweighted R value based on all observations decreased from 10.6 to 8.4%. A redetermination of the structure at 120 K concluded the analysis.

1. Introduction

Single crystal diffractometry is used to determine crystal structures. It is tacitly assumed that these structure models are *e.g.* device independent. However, as pointed out previously (Rousseau *et al.*, 2000; Lenstra & Rousseau, 1999), a simple change in tube voltage suffices to produce, on the same instrument, a systematic shift in the ADP (atomic displacement parameter) values. Using Mo radiation and working with standard equipment, *i.e.* non-synchrotron radiation, one finds for the isotropic displacement parameter: $B(\text{model}) > B(\text{true})$. The bias in B is the result of systematic intensity errors caused by a mismatch between the applied scan width and the wavelength dispersion in the monochromated X-ray beam.

Of course, we are not only interested in the systematic intensity errors. Random errors on the net intensities are also important. The traditional background–peak–background

(BPB) procedure leads in our opinion to a set of $\sigma^2(I)$ values that is at best a zero-order approximation for the real random errors. To illustrate our point we formulate in §2 a background model in the form of a θ-dependent polynomial. This summary of all background observations $B(\underset{\sim}{H})$ is in line with previous publications (Maes *et al.*, 1998; Lenstra, Geise & Vanhouteghem, 1991; Lenstra, Verbruggen *et al.*, 1991; Eisenstein & Hirshfeld, 1983). The subtraction of the local background B from the raw intensity R leads to $I = R - B$. Therefore, the BPB variance for $I_{\rm net}$ is equal to $R + B$; this value reduces to I when the background model is applied. In this way it is possible to reduce the practical detection limit $\sigma(I)$ of the local diffraction equipment by one order of magnitude.

We decided to use the structures of copper(II) hydrogenmalonate dihydrate (henceforth abbreviated as CuHM) and manganese(II) hydrogenmalonate dihydrate (MnHM) in an analysis of the reproducibility of a crystal structure. A graphite-monochromated Mo $K\alpha$ beam has a wavelength dispersion $\Delta\lambda/\lambda$ of 0.14 on our CAD-4/stationary anode device. $\Delta\lambda/\lambda$ reduces to 0.09 on our Mach3/rotating anode equipment (Lenstra *et al.*, 1998). In §3 we look at the difference between the CuHM structures refined with CAD-4 and Mach3 intensities. We observe significant changes in the ADP's. The analysis of the isomorphous structure of MnHM illustrates that the geometrical variations linked to the Jahn–Teller effect in CuHM are readily observed, regardless of the instrumental uncertainties in the ADP's.

In §4 we look at the robustness of the CuHM and MnHM structure models. When we divide the original data sets into low-order (LO) data ($0 < \theta < 30^\circ$) and high-order (HO) data ($30 < \theta < 45^\circ$), we find significant differences. HO and LO scale factors exclude each other showing a 10% loss in absolute intensities between LO and HO data. That difference is not only device, but also compound independent. This model inconsistency is in our opinion in keeping with the above-mentioned intensity truncation error (Rousseau, Maes & Lenstra, *loc. cit*).

The presence of pseudo I-centred sublattices in the CuHM framework is not without consequence. Model variations were observed by refining the CuHM structure on intensity data with $(h + k + l) = 2n$ and $2n + 1$, respectively. Our selection of observed intensities $[I > 3\sigma(I)]$ stresses the pseudo-symmetry.

In §5 we apply the background model in the calculation of the net intensities and their errors. It remedies the shortcomings caused by the above-mentioned data selection and yields a more balanced structure model.

The structures of CuHM and MnHM are discussed in §6. Although the metal coordination is the same as in magnesium hydrogen malonate dihydrate (Briggman & Oskarsson, 1978), the packing of the present structures proved to be completely different.

It is difficult to assess the quality of the changes in the structure model caused by the proposed background elimination procedure. We felt that an experimental check was possible *via* a low-temperature study. This approach, in which the BPB procedure is retained, also leads to a significant increase in the number of intensities with $I > 3\sigma\ (I)$. The low-temperature analysis is described in §7. The results support our preference for background modelling above the traditional BPB procedure.

Conclusions are drawn in §8.

2. Background modelling

In general, we calculate net intensities I with the background–peak–background (BPB) procedure. Here I is obtained by subtracting the local background $B(\underset{\sim}{H})$ from the raw intensity $R(\underset{\sim}{H})$. Since R and B are independent observations we have

$$I = R - \gamma B \text{ and } \sigma^2(I) = \sigma^2(R) + \gamma^2\sigma^2(B),$$

where γ is the ratio of the times spent in measuring R and B per Bragg position. On our local equipment $\gamma = 2$. Each reflection is observed in a step scan procedure involving 96 steps along the scan direction. A uniform scan speed is employed. The first and last 16 steps are indicative for the local background. The integrated intensity over the central 64 steps gives the raw intensity R. For weak intensities, *i.e.* $R \simeq \gamma B$, $\sigma^2(I)$ is almost entirely determined by the background. Counting statistics lead to $\sigma^2(I) \simeq \gamma(1 + \gamma)B$. As demonstrated previously (Maes *et al.*, 1998; Lenstra, Geise & Vanhouteghem, 1991; Lenstra, Verbruggen *et al.*, 1991) we can reduce $\sigma^2(I)$ to I, *i.e.* the variance on $I_{\rm net}$ is background independent, because all observations $B(\underset{\sim}{H})$ are interrelated.

The observed background is produced by three scattering processes, *viz*.

(i) elastic Rayleigh scattering with $B_R \simeq f^2$;

(ii) inelastic Compton scattering with $B_C \simeq (Z - f^2/Z)$, where Z is the atomic number of the scatterer;

(iii) pseudo-elastic or thermal diffuse scattering with $B_{\rm TDS} \simeq f^2\ (1 - \exp[-2Bs^2])$.

This illustrates immediately that the background intensity is a continuous function of the scattering angle θ. This allows us to represent the background *via* a Taylor series. To summarize all our observations $B(\underset{\sim}{H})$ we used an 11th degree polynomial in θ, *viz*.

$$B(\theta) = \sum_{i=0}^{11} (\theta - \theta_{\rm min})^i,$$

in which $\theta_{\rm min}$ was the minimum Bragg angle in the data set. This description is similar to the one presented by Eisenstein & Hirshfeld (1983). We calculated average B values for θ intervals of 0.25° from $\theta = 2^\circ$ up to $\theta = 45^\circ$. The coefficients a_i were adjusted to $\langle B(\theta)\rangle$ *via* a least-squares analysis. The R value, which was defined as

$$R = \left\{ \sum_\theta N_{\rm obs}(B_{\rm model} - \langle B_{\rm obs}\rangle)^2 / \sum_\theta N_{\rm obs}\langle B_{\rm obs}\rangle^2 \right\}^{1/2},$$

converged to 0.02. Here $N_{\rm obs}$ is the number of observed reflections per θ shell.

The polynomial $B(\theta)$ predicts the local background b for each individual reflection. The Bragg intensity is superimposed on that background value b. Since the accuracy of b is linked to $\Sigma B(\underset{\sim}{H})$, the predicted background b is practically

Table 1
The reconstruction of the intensity signal from the observation R and an 'ideal' background of 50 counts.

The variance σ^2 $(i|R,b) = \langle i|R,b\rangle$.

R	$\langle r\|R\rangle$	$\sigma^2(r\|R)$	$\langle B\|b\rangle$	$\sigma^2(B\|b)$	$\langle i\|R,b\rangle$
31	51.33	3.96	29.67	2.63	1.33
41	52.68	9.77	38.32	7.10	2.68
51	55.66	24.64	45.34	18.99	5.66
61	61.87	50.64	49.13	38.77	11.87
71	71.00	71.00	50.00	50.00	21.00
81	81.00	81.00	50.00	50.00	31.00

error free. Therefore, the accuracy of the expected background b is superior to that for the observed value. The chance to observe the latter is easily calculated from the counting statistical distribution $P(B|b)$, in which b serves as the average and variance.

Since the background B and the signal I are unrelated we have: $P(R) = P(B)P(I)$. The distribution $P(R)$ is known as the result of the experimental measured value of $R(H)$. The background distribution $P(B|b)$ is known *via* the background model $B(\theta)$. Consequently

$$P(I) = P(R)/P(B|b) \text{ and thus: } I = R - b \text{ and } \sigma^2(I) = I.$$

To avoid complications with *e.g.* negative intensities we decided to evaluate small intensities using a Bayesian approach. The true value r of the raw intensity is linked to the actual observation R *via*

$$P(r|R) = P(R|r)P(r).$$

The likelihood is that $P(R|r)$ is a counting statistical distribution with an average and variance equal to r. The prior distribution $P(r)$ expresses our experience or our expectation. In the absence of specific information we have $P(r) = 0$, if $r < 0$ and otherwise $P(r)$ is a uniform distribution. The first moment of the posterior distribution $P(r|R)$ replaces the actual observation R. We find $\langle r|R\rangle = R + 1$, which is in our view the basis behind the working practice in the reflection profile analysis presented by Blessing (1987).

In the absence of any experience [a uniform $P(r)$] the experiment is decisive. In the presence of detailed knowledge – in our current analysis the background model – it is the prior that (co) determines the posterior moments. In our intensity calculation we divide the observation R into the hypothetical observations B and I with the logical restriction that $(B + I) = R$. At the same time b and the true intensity i can be substituted for r. This gives

$$P(r|R) = P(I|i)P(i)P(B|b)P(b).$$

The prior $P(b)$ is a δ function, because the error on b is negligible. $P(B|b)$ and $P(I|i)$ are counting statistical distributions defined by b and i. The prior $P(i)$ is a uniform distribution for $i \geq 0$, whereas $P(i) = 0$ for $i < 0$.

The impact of this analysis on raw intensities R with $b - 4(b)^{1/2} < R < b + 4(b)^{1/2}$ is illustrated in Table 1. The ideal background b was set at 50 counts. As we can see the posterior moment of $P(r|R)$ exceeds that b value. The net intensity is given by $(\langle r|R\rangle - b)$. This value is equal to $R - \langle B|b\rangle$, in which $\langle B|b\rangle$ is calculated as the first moment $\langle B|b\rangle = \int_o^R BP(B|b)\mathrm{d}B$.

Therefore, as an example, a raw intensity R of 41 counts contains a background component of 38.3 counts. The variance on that background intensity is 7.1. The posterior moment $\langle r|R\rangle$ for the observation of 41 counts in R is equal to 52.7 counts. The second moment about the mean $\sigma^2(r|R) = 9.8$. Since $P(i|I) = P(I|i)P(i) = P(r|R)/P(B|b)$ we find $\sigma^2(i|I) = 9.8–7.1 = 2.7$.

3. Experimental and refinement

Crystals of CuHM and MnHM were grown by slow evaporation of an aqueous solution prepared by dissolving stoichiometric amounts of malonic acid and the metal carbonate in water. To determine the structure of the copper compound we measured reflection intensities on our CAD-4 diffractometer. A stationary anode served as the X-ray source. In the initial experiment we used a fine-focus Mo-tube operated at 20 mA and 50 kV. The take-off angle of the tube was set at 2.9°, thus

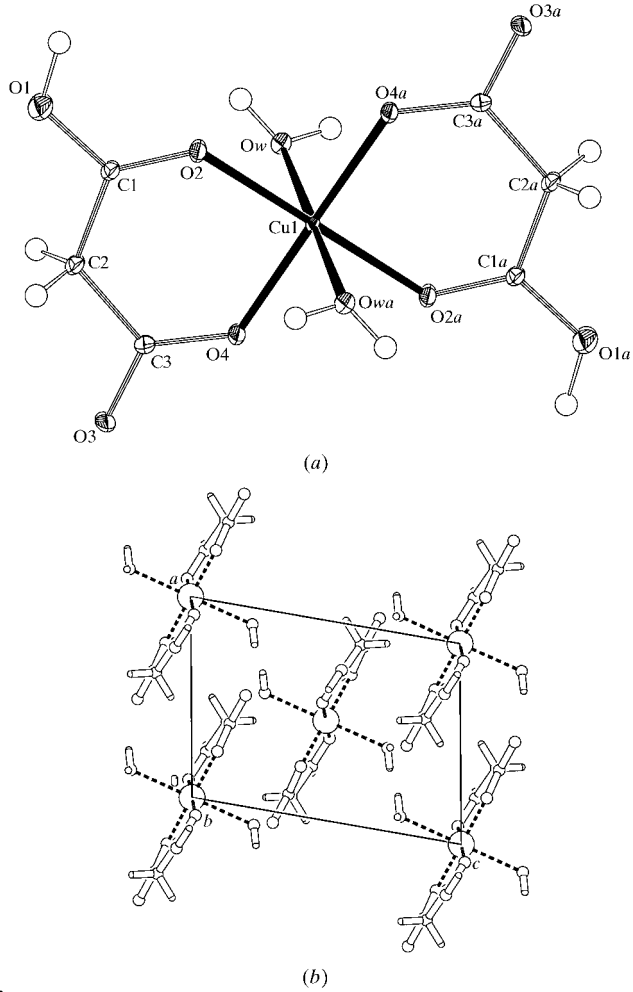

Figure 1
(*a*) Atomic numbering scheme in CuHM. (*b*) The packing of CuHM projected along the monoclinic b axis.

Table 2
Experimental details.

	Cu CAD-4 294 K	Cu CAD-4 120 K	Mn CAD-4 294 K	Cu Mach3 294 K	Cu CAD-4 294 K second crystal
Crystal data					
Chemical formula	$C_6H_{10}CuO_{10}$	$C_6H_{10}CuO_{10}$	$C_6H_{10}MnO_{10}$		
Chemical formula weight	305.68	305.68	297.08		
Cell setting, space group	Monoclinic, $P2_1/n$	Monoclinic, $P2_1/n$	Monoclinic, $P2_1/n$		
a, b, c (Å)	7.0655 (7), 7.5017 (8), 9.676 (1)	7.019 (2), 7.472 (2), 9.498 (2)	7.0909 (7), 7.3518 (7), 9.577 (1)		
β (°)	100.88 (2)	99.94 (2)	99.73 (2)		
V (Å^3)	503.6 (2)	490.7 (4)	492.1 (2)		
Z	2	2	2		
D_x (Mg m^{-3})	2.02	2.07	2.00		
Radiation type	Mo $K\alpha$	Mo $K\alpha$	Mo $K\alpha$		
No. of reflections for cell parameters	25	25	25		
θ range (°)	10.0–23.0	10.1–23.0	12.0–28.0		
μ (mm^{-1})	2.216	2.275	1.390		
Temperature (K)	294	120	294		294
Crystal form, colour	Prism, blue	Prism, blue	Prism, pink		Prism, blue
Crystal size (mm)	0.20 × 0.20 × 0.20	0.40 × 0.20 × 0.20	0.1 × 0.1 × 0.1		0.4 × 0.2 × 0.2
Data collection					
Tube setting	20 mA/50 kV	20 mA/50 kV	20 mA/50 kV	30 mA/50 kV	20 mA/50 kV
Size focal spot (mm^2)	0.4 × 0.4	0.4 × 0.4	0.4 × 0.4	0.3 × 0.3	0.4 × 0.4
Diffractometer	Enraf–Nonius CAD-4	Enraf–Nonius CAD-4	Enraf–Nonius CAD-4	Enraf–Nonius Mach3	Enraf–Nonius CAD-4
Data collection method	$\omega/2\theta$ scans	$\omega/2\theta$ scans	$\omega/2\theta$ scans	$\omega/2\theta$ scans	$\omega/2\theta$ scans
Scan angle (°)	0.8 + 2.0tan θ	0.8 + 2.0tan θ	0.8 + 2.0tan θ	0.8 + 2.0tan θ	0.8 + 2.0tan θ
Max. scan time (s)	120	120	120	120	120
Absorption correction	Psi scan	Psi scan	Psi scan	Psi scan	Psi scan
T_{min}	0.90	0.8000	0.94	0.905	0.850
T_{max}	1.0	1.0000	0.999	0.999	0.999
No. of measured, independent and observed parameters	4333, 4117, 4117	4248, 4248, 2972	5395, 5395, 2085	4340, 4340, 2199	1462, 1462, 1153
Criterion for observed reflections	$I > 0.0\sigma(I)$	$I > 3\sigma(I)$	$I > 3\sigma(I)$	$I > 3\sigma(I)$	$I > 3\sigma(I)$
θ_{max} (°)	45	45	50	45	30
Range of h, k, l	$0 \rightarrow h \rightarrow 14$ $0 \rightarrow k \rightarrow 14$ $-19 \rightarrow l \rightarrow 19$	$0 \rightarrow h \rightarrow 14$ $0 \rightarrow k \rightarrow 14$ $-19 \rightarrow l \rightarrow 19$	$0 \rightarrow h \rightarrow 15$ $0 \rightarrow k \rightarrow 15$ $-20 \rightarrow l \rightarrow 20$	$0 \rightarrow h \rightarrow 14$ $0 \rightarrow k \rightarrow 14$ $-19 \rightarrow l \rightarrow 19$	$0 \rightarrow h \rightarrow 9$ $0 \rightarrow k \rightarrow 10$ $-13 \rightarrow l \rightarrow 13$
No. and frequency of standard reflections	3 every 120 min	3 every 120 min	3 every 120 min	3 every 120 min	
Refinement					
Refinement on	F	F	F	F	F
R, wR, S	0.083, 0.064, 4.108	0.048, 0.052, 4.862	0.06, 0.051, 3.561	0.041, 0.040, 3.146	0.032, 0.035, 3.746
No. of reflections and parameters used in refinement	4117, 99	2972, 99	2085, 99	2199, 99	1153, 99
H-atom treatment	All H-atom parameters refined	All H-atom parameters refined	All H-atom parameters refined	All H-atom parameters refined	All H-atom parameters refined
Weighting scheme	σ	σ	σ	σ	σ
$(\Delta/\sigma)_{max}$	0.05	0.033	0.018	0.02	0.25
$\Delta\rho_{max}$, $\Delta\rho_{min}$ (e Å^{-3})	1.088, −1.835	1.924, −2.316	1.66, −1.915		

Computer programs used: *CAD*-4 (Enraf–Nonius, 1994), *MolEN* (Fair, 1990), Patterson and Fourier, *LSFM* in *MolEN* (Fair, 1990), *BTABLE* in *MolEN* (Fair, 1990).

generating a focal spot of 0.4 × 0.4 mm. The incident X-ray beam was monochromated with a pyrolytic graphite crystal.

Experimental details are summarized in Table 2.[1] Reflection intensities were measured in the $\omega/2\theta$ scan mode with a scan angle ω of $(0.8 + 2.0\tan\theta)^\circ$. The mosaicity of the CuHM crystal was measured with a narrow vertical slit in front of a stationary detector. A rotation of the crystal over 1.1° in ω was required. Therefore, we measured intensities with an aperture of 4.5 mm, *i.e.* with a detector opening of 1.3°. Intensity control reflections were used to calculate the experimental spread s^2 and the average intensity $\langle I\rangle$. This allowed the calculation of the instrumental instability p over the measuring period *via* $s^2 = \sigma^2 + (pI)^2$. Here σ^2 is the counting statistical variance; its value equals $\langle I\rangle$. We found $p = 0.01$.

Systematic extinct reflections pointed at the space group $P2_1/n$. The crystal structure was solved using Patterson and

[1] Supplementary data for this paper are available from the IUCr electronic archives (Reference: LC0029). Services for accessing these data are described at the back of the journal.

Table 3

(*a*) Atomic coordinates and isotropic atomic displacement parameters (IDP) for CuHM at 294 K.

$B_{eq} = (4/3)[a^2\beta^{11} + b^2\beta^{22} + c^2\beta^{33} + (2ac\cos\beta)\beta^{13}]$.

				Mach 3 + BPB	Mach 3 + background model	CAD-4	CAD-4 $h+k+l=2n$	CAD-4 $h+k+l=2n+1$
	x	*y*	*z*	*B* (Å^2)	*B* (Å^2)	*B* (Å^2)	*B* (Å^2)	*B* (Å^2)
Cu1	1.000	0.000	1.0000	1.585 (4)	1.597 (4)	1.433 (5)	1.460 (4)	0.7 (2)
O1	0.7334 (2)	0.4888 (2)	0.9444 (2)	3.09 (3)	2.82 (3)	3.37 (4)	2.95 (3)	2.1 (2)†
O2	0.9136 (2)	0.2478 (2)	1.0133 (1)	2.02 (2)	2.03 (2)	1.89 (3)	1.92 (3)	1.92 (5)
O3	0.4455 (2)	−0.0607 (2)	0.7997 (2)	2.68 (3)	2.70 (2)	2.57 (4)	2.58 (3)	2.70 (6)
O4	0.7487 (2)	−0.0813 (2)	0.9060 (1)	1.90 (2)	1.91 (2)	1.81 (3)	1.81 (3)	1.86 (5)
O*w*	1.0838 (2)	0.0883 (2)	0.7721 (2)	2.17 (2)	2.15 (2)	2.04 (4)	2.04 (3)	2.17 (5)
C1	0.7608 (2)	0.3141 (2)	0.9471 (2)	1.43 (3)	1.41 (2)	1.31 (4)	1.34 (3)	1.48 (7)
C2	0.5964 (3)	0.2094 (2)	0.8649 (2)	2.48 (4)	2.50 (3)	2.37 (5)	2.39 (4)	2.56 (8)
C3	0.5994 (2)	0.0098 (2)	0.8578 (2)	1.52 (2)	1.50 (2)	1.40 (3)	1.44 (2)	2.7 (2)
H1*w*	1.077 (3)	0.179 (3)	0.757 (2)	3.3 (5)‡	3.9 (5)‡	4 (1)‡	4 (1)‡	3 (1)‡
H21	0.566 (4)	0.244 (4)	0.783 (3)	6.2 (7)‡	7.8 (9)‡	12 (2)‡	7 (1)‡	6 (1)‡
H2*w*	1.190 (4)	0.049 (3)	0.779 (3)	3.7 (6)‡	3.8 (5)‡	3.2 (9)‡	4 (1)‡	3 (1)‡
H22	0.481 (5)	0.240 (5)	0.926 (4)	10 (1)‡	10 (1)‡	11 (2)‡	6 (1)‡	6 (1)‡
H11	0.839 (5)	0.578 (5)	1.005 (3)	6.9 (8)‡	7.2 (9)‡	6 (2)‡	6.0‡§	6.0‡§

(*b*) Coordinates and isotropic displacement parameters for MnHM at 294 K

	x	*y*	*z*	*B* (Å^2)
Mn1	1.000	0.000	1.0000	1.147 (6)
O1	0.7244 (3)	0.5025 (3)	0.9372 (2)	3.52 (4)
O2	0.8972 (2)	0.2574 (2)	1.0158 (2)	2.36 (3)
O3	0.4367 (2)	−0.0615 (3)	0.7943 (2)	2.61 (3)
O4	0.7411 (2)	−0.0796 (2)	0.8926 (2)	2.17 (3)
O*w*	1.0897 (2)	0.0888 (2)	0.8033 (2)	2.17 (3)
C1	0.7477 (3)	0.3237 (3)	0.9466 (2)	1.70 (4)
C2	0.5813 (3)	0.2145 (3)	0.8719 (3)	2.25 (4)
C3	0.5909 (3)	0.0111 (3)	0.8533 (2)	1.67 (3)
H1*w*	1.061 (7)	0.203 (8)	0.739 (4)	12 (2)‡
H21	0.538 (4)	0.276 (4)	0.782 (3)	3.8 (7)‡
H2*w*	1.205 (4)	0.041 (5)	0.786 (3)	4.9 (8)‡
H22	0.453 (5)	0.241 (6)	0.898 (4)	8 (1)‡
H11	0.878 (6)	0.590 (6)	0.980 (4)	8 (1)‡

(*c*) Coordinates and IDP's for CuHM at 120 K

	x	*y*	*z*	*B* (Å^2)
Cu1	1.000	0.000	1.0000	0.587 (3)
O1	0.7349 (2)	0.4922 (2)	0.9413 (2)	1.37 (2)
O2	0.9139 (2)	0.2499 (2)	1.0125 (1)	0.86 (2)
O3	0.4444 (2)	−0.0620 (2)	0.7988 (2)	1.16 (2)
O4	0.7487 (2)	−0.0814 (2)	0.9050 (1)	0.83 (2)
O*w*	1.0846 (2)	0.0874 (2)	0.7725 (2)	0.92 (2)
C1	0.7605 (2)	0.3165 (2)	0.9467 (2)	0.64 (2)
C2	0.5921(2)	0.2106 (2)	0.8687 (2)	1.02 (3)
C3	0.5986 (2)	0.0093 (2)	0.8581 (2)	0.67 (2)
H1*w*	1.079 (5)	0.200 (5)	0.760 (4)	3.4 (8)‡
H21	0.563 (4)	0.255 (4)	0.771 (3)	2.2 (6)‡
H2*w*	1.175 (6)	0.042 (5)	0.764 (4)	3.3 (8)‡
H22	0.481 (4)	0.235 (4)	0.927 (3)	2.2 (6)‡
H11	0.840 (4)	0.568 (4)	0.995 (3)	1.2 (5)‡

† Atomic displacement parameter for O1 is not positive-definite. ‡ These atoms were refined isotropically. § Not refined.

Fourier methods. ψ scans were used to correct the reflection intensities for absorption (North *et al.*, 1968). Reflections were weighted according to $[\sigma^2 + (pI)^2]^{-1}$. The non-H atoms were refined anisotropically. The H atoms, located from a difference electron density map, were refined isotropically. Only intensities with $I > 3\sigma(I)$ were included in the refinement. The atomic numbering scheme is illustrated in Fig. 1(*a*). Fig. 1(*b*) depicts the packing projected on the *ac* plane. Final values for the atomic coordinates and the B_{eq} values are given in Table 3.

The CuHM crystal was transferred from the CAD-4/stationary anode device with a focal spot of 0.4 × 0.4 mm to the Mach3/rotating anode equipment with a focus of 0.3 × 0.3 mm. The reduction in focal spot size limits the divergence of the X-ray beam impinging upon the monochromator. The reduction in divergence causes a decrease in $\Delta\lambda/\lambda$, which shifts from 0.14 (CAD-4) to 0.09 (Mach3) (see Lenstra *et al.*, 1998).

The CAD-4 scan parameters were used for the Mach3 experiment. The ratio between the scale factors (on *F*) of 0.766 (Mach3)/0.585 (CAD-4) matches the difference in tube current (see Table 2). The difference in beam intensity ought to reduce the Mach3 e.s.d.'s to 0.8 times the e.s.d.'s of the CAD-4. This effect is reinforced by the increase in the number of intensities $I > 3\sigma(I)$ from 1910 (CAD-4) to 2199 (Mach3).

The symmetry-independent intensities of MnHM were collected on the CAD-4 diffractometer [aperture 4 mm, mosaicity 1° in ω, $\omega/2\theta$ scan mode, ω scan width $(0.8 + 2.0\tan\theta)^\circ$]. The structure, which is isomorphous with CuHM, was refined using 2532 reflections with $I > 3\sigma$. The results are summarized in Table 3(*b*).

Before analyzing the geometrical details of the structures, we will look critically at our *modus operandi*. Differentation of Bragg's law $-2d\sin\theta = \lambda -$ leads to $\Delta\theta = (\Delta\lambda/\lambda)\tan\theta$. This links the angular width of the

reflection with the wavelength dispersion in the incident X-ray beam. In our software we use the scan angle expression ($a + b$ tan θ)$^\circ$ with $b = (\Delta\lambda/\lambda)(360^\circ/2\pi)$. In our experiments ($b$ = 2.0) we assumed a wavelength dispersion of 0.035 as characteristic for the incident X-ray beam. So, the selected scan angle underestimates the real wavelength windows of ~14 and 9% present on the stationary anode/CAD-4 equipment and the rotating anode/Mach3 device, respectively. Consequently X-ray models become biased (Rousseau *et al.*, 2000). Since $\Delta\lambda/\lambda$ is smaller on the Mach3, we expect B(Mach3) to be closer to B(true) than the corresponding values for B(CAD-4). This idea was tested in an earlier stage using a crystal of ammonium hydrogen tartrate (van Bommel & Bijvoet, 1958). The B_{eq} values, averaged over the non-H atoms, were 1.97 and 1.82 Å^2 for the CAD-4 and Mach3 measurements, respectively (Maes, 1997). The decrease in B is the consequence of smaller intensity truncation errors. In this work we found the opposite for CuHM: B(Mach3) > B(CAD-4).

This surprising result is caused by an intensity truncation error dictated by the aperture of 4.5 mm. On the Mach3 we had installed the extension arm, thereby doubling the crystal-to-detector distance from 208 to 403 mm. To deal with the mosaicity we needed a detector opening of 9 mm which was not available. By using a slit of 4.5 mm we introduced an additional source of intensity truncation, which is not detectable in the residual values, because the intensity truncation is absorbed in the ADP's. Randomization of systematic intensity errors, however, prevents us obtaining S values close to 1, because the least-squares Δ's do not reflect the random errors $s(I)$ typical for the experiments. In our opinion S is more informative than it is often given credit for. The selection of intensities to be included in the refinement is another element to consider. Often data are selected *via* a criterion such as $I > 3\sigma(I)$. The omission of weak intensities causes a bias in the structure model (Hirshfeld & Rabinovich, 1973). Therefore, many crystallographers prefer a complete data set as the starting point in the least-squares analysis. Refinements on I have made it possible to incorporate negative intensities in the calculations. This working practice is in our opinion valid when the data set is measured with *e.g.* an area detector. We employed a point detector. In order to save time during the data collection we used the following measuring strategy. When the preliminary reflection scan, with a speed of 5.5° min^{-1}, resulted in a ratio for $I/\sigma < 0.33$ the final scan of 120 s was omitted. Here σ is calculated following the BPB procedure. This time-saving strategy creates a serious bias in the set of the smallest observed intensities (Lenstra, Geise & Vanhouteghem, 1991). A selection criterion such as $I > 3\sigma$ has the advantage that the subset of data used in the refinement contains only unbiased information.

4. Lack of model robustness

4.1. Impact of intensity truncation errors

Variations in the structure model become clearly visible, when we divide the intensity data for CuHM and MnHM into a low-order (LO) data set with $s < 0.7$ Å^{-1} and a high-order (HO) data set with $0.7 < s < 1.0$ Å^{-1}. Between the original full angle model and the LO and the HO model we noticed insignificant shifts in atomic coordinates. Significant shifts are found in the atomic displacements. Such behaviour can be expected using spherical atoms in the structure optimization. The B_{eq} values of the LO and HO model are tabulated in Table 4. The ADP's in the HO models are smaller than those obtained in the optimization with LO data. The latter values are close to the full angle (FA) results listed in Table 3.

The extreme variation in B_{eq} (O1) is peculiar. Its value shifts roughly by 1 Å^2 when we go from the LO to the HO refinements. This variation does not only occur in the CAD-4 and Mach3 inferred model for CuHM, but also in that for MnHM. LO and HO models also show significantly different values for scale factors. The CAD-4 measurements for CuHM lead to scale factors (on F) of 0.616 (1) and 0.583 (1) for HO and LO refinements, respectively. This indicates a 10% loss in absolute intensity for the HO data compared with the LO data. A similar intensity loss is suggested by the Mach3 data with scale factors of 0.810 (1) (HO) and 0.763 (1) (LO). Both HO and LO scale factors, *viz*. CAD-4 *versus* Mach3 values, are in keeping with the applied tube currents of 20 and 30 mA. The LO and HO scale factors for the manganese(II) derivative reveal the same pattern, *i.e.* the LO data are ~10% more intense than the HO data. The difference between the HO and LO scale factor is of the same magnitude as the systematic intensity errors by the scan-angle-induced spectral truncation error. For the analysis of this intensity error of 10% we refer to Rousseau *et al.* (2000). The correlation between scale factors and B values is in our view an additional element in the explanation of the variation in B_{eq}.

4.2. Impact of pseudo-symmetry

The intensity distribution function based on all observations points to a centrosymmetric space group. The moments of the distribution function are shown in Table 5. For the data with $(h + k + l) = 2n$ we find $\langle E^2 \rangle = 1.75$. This is clearly related to the Cu sublattice, which is almost I-centred. We continued our analysis by splitting the original measurements into two subsets of data with the same resolution dividing the reflections according to $(h + k + l) = 2n$ (even) or $2n + 1$ (odd). The latter subset contains primarily small intensities, because the contribution of the Cu sublattice to I_{obs} is very small. Only the anisotropic temperature factor β(Cu) breaks the I-centring of the metal sublattice. The intensity distribution in the data set odd is hypercentric (see Table 5). The distribution of E's in the even data set is practically acentric. This is the consequence of the dominant Cu contribution to the structure amplitudes.

Both data sets – odd and even – were used to refine the CuHM structure. The effective number of reflections with $I > 3\sigma$ was 392 and 1518 observations in odd and even, respectively. This means that σ(odd) should be twice σ(even). As can be seen in Table 3 this holds for all e.s.d.'s except for those on B_{eq} for Cu, O1 and C3. Moreover, the B_{eq} values for these three atoms show large discrepancies between even and

Table 4
The variation in B_{eq} values caused by differences in the scenarios of the refinement.

In the HO refinements the parameters of H atoms were fixed to their LO values. Bck: background model replaced the BPB procedure.

	Second Cu crystal CAD-4 B (Å^2)	Cu CAD-4 HO B (Å^2)	Cu CAD-4 LO B (Å^2)	Cu mach3 HO B (Å^2)	Cu mach3 LO B (Å^2)	Cu mach3 bck HO B (Å^2)	Cu mach3 bck LO B (Å^2)	Mn CAD-4 HO B (Å^2)	Mn CAD-4 LO B (Å^2)
M	1.499 (6)	1.386 (4)	1.455 (8)	1.509 (3)	1.599 (6)	1.532 (5)	1.594 (8)	1.154 (3)	1.150 (9)
O1	3.12 (4)	2.19 (3)	3.13 (5)	2.33 (2)	3.20 (4)	2.28 (3)	3.04 (5)	2.27 (2)	3.67 (6)
O2	1.91 (3)	1.89 (3)	1.87 (4)	1.93 (2)	2.04 (3)	1.94 (3)	2.04 (4)	1.95 (2)	2.41 (5)
O3	2.58 (4)	2.55 (5)	2.53 (5)	2.68 (3)	2.69 (4)	2.68 (4)	2.71 (4)	2.18 (3)	2.66 (5)
O4	1.81 (3)	1.68 (3)	1.78 (4)	1.80 (2)	1.92 (3)	1.81 (3)	1.93 (4)	1.71 (2)	2.23 (5)
O*w*	2.08 (3)	1.95 (4)	2.04 (4)	2.03 (2)	2.19 (3)	1.97 (3)	2.19 (4)	1.79 (2)	2.22 (5)
C1	1.36 (4)	1.28 (3)	1.31 (5)	1.35 (2)	1.47 (4)	1.30 (2)	1.47 (4)	1.33 (2)	1.78 (6)
C2	2.37 (5)	2.42 (4)	2.35 (6)	2.49 (3)	2.48 (5)	2.48 (4)	2.53 (6)	1.92 (3)	2.31 (7)
C3	1.43 (4)	1.36 (2)	1.38 (4)	1.46 (2)	1.54 (4)	1.43 (2)	1.54 (5)	1.28 (2)	1.75 (5)
H1*w*	3.6 (7)†		2.9 (8)†		3.3 (7)†		3.3 (8)†		12 (2)†
H21	5.8 (9)†		6 (1)†		6 (1)†		8 (1)†		4.0 (9)†
H2*w*	3.9 (7)†		4 (1)†		4.0 (8)†		4.2 (9)†		5 (1)†
H22	8 (1)†		9 (2)†		10 (1)†		11 (2)†		8 (2)†
H11	8 (1)†		7 (1)†		7 (1)†		7 (1)†		8 (2)†
(*b*)									
R_1	0.032	0.051	0.037	0.041	0.033	0.147	0.045	0.058	0.047
R_2	0.035	0.040	0.041	0.033	0.039	0.113	0.067	0.048	0.049
S	3.746	1.139	4.367	1.041	4.042	3.433	6.582	1.043	4.684
NV	99	79	99	79	99	79	99	79	99
No. $I > 3\sigma$	1153	803	1107	1022	1177	2679	1546	1436	1096
SFOBS‡	0.695	0.616	0.583	0.810	0.763	0.801	0.760	1.245	0.975
Refl.	1462	2801	1548	2787	1546	2679	1546	6046	1551

† H atoms were refined isotropically. ‡ SFOBS represents the scale factor with e.s.d.'s of 0.001.

odd. β(Cu), from which B_{eq} (Cu) was calculated, see heading to Table 3, breaks the I-centring in the Cu sublattice. Its small impact on I(odd) makes β(Cu) difficult to determine. This explains the large e.s.d. for B_{eq} (Cu|odd). The same holds for O1 and C3. Both atoms have y coordinates very close to 0 or $\frac{1}{2}$. O1 and C3 also form pseudo-I-centred sublattices *via* the equivalent positions (x, y, z) and $(\frac{1}{2} + x, \frac{1}{2} - y, \frac{1}{2} + z)$.

During the refinement the Cu coordinates were fixed at (1, 0, 1) for symmetry reasons. Such symmetry restrictions do not apply to O1 and C3. The positional errors for these two atoms are in line with $\sigma(B_{eq})$, *i.e.* the positional uncertainty increases by one order of magnitude when we go from the even model to the odd one. The correlation between position and ADP in the odd model is large for O1 and C3. The relevant coefficients exceed 0.8. In the even model these correlation coefficients are smaller than 0.6.

The pseudo-symmetry in the crystal structures of CuHM and MnHM clearly causes complications in the modelling process. We find for O1 B_{eq} values of 2.1 (2) Å for $(h + k + l) = 2n + 1$ and 2.95 (3) Å^2 for $(h + k + l) = 2n$. This difference is of the same magnitude as the discrepancy between B(O1|HO) and B(O1|LO).

When we compare the results of the odd and even structure analyses we do not expect to find a difference in scale factors, because the intensity truncation errors affect both data sets in the same way. We find scale factors of 0.578 (2) and 0.586 (1) for odd and even, respectively. This suggests a 3% discrepancy in intensity. In view of the e.s.d.'s we do not feel that this difference is significant.

To complete our analysis of reproducibility we redetermined the crystal structure of CuHM using a different crystal. We collected a data set up to $\theta = 30^\circ$ on our CAD-4 diffractometer. The mosaicity of the crystals was measured. An ω rotation of 1° was sufficient. Therefore, scan angle and aperture were taken to be identical to the previous values. As can be seen in Table 4 the refined structure is practically identical to the LO structure of the first analysis. O1 again underlines its special character by showing a shift of 5 e.s.d.'s in its B_{eq} value. The C1—O1 bond distance converged at 1.321 (3) Å, *i.e.* a value close to the distance inferred from the Mach3 data set. The least-squares optimized scale factor of 0.695 (1) matches the scale factor of the earlier CAD-4 measurements [0.585 (1)] given the difference in volume of the crystal (see Table 2).

5. Application of background model

In the initial refinement of the CuHM structure with the Mach3 data set we used net intensities calculated with the BPB procedure. With 2199 observations for which $I > 3\sigma(I)$ we arrived at a weighted R value of 0.041. The weights were given by $[\sigma^2 + (0.01I)^2]^{-1}$. The S value of 3.15 indicates that we have a serious discrepancy between the least-square Δ's and the random errors s. This discrepancy is in our view the consequence of the systematic intensity errors in the CuHM data. The scan-angle-induced truncation error goes up to ~10% at $\theta = 45^\circ$ (see Rousseau *et al.*, 2000), *i.e.* the systematic error exceeds the random error. The randomization of the

Table 5
Moments of the experimental intensity distribution for CuHM at room temperature observed with the CAD-4 diffractometer for data sets with $h + k + l = 2n$ (even), $h + k + l = 2n + 1$ (odd) and all data combined.

	Experimental			Theory		
Moment of $P(E)$	Even	Odd	Odd + even	Acentric	Centric	Hypercentric
$\|E\|$	0.814	0.666	0.786	0.886	0.798	0.718
$\|E\|^2$	1.000	1.000	1.000	1.000	1.000	1.000
$\|E\|^3$	1.424	1.886	1.550	1.329	1.596	1.916
$\|E\|^4$	2.266	4.206	2.735	2.000	3.000	4.500
$\|E\|^5$	3.939	10.664	5.303	3.323	6.383	12.260
$\|E\|^6$	7.355	29.920	11.069	6.000	15.000	37.500
$\|\|E\|^2 - 1\|$	0.839	1.163	0.967	0.736	0.968	1.145
$(\|E\|^2 - 1)^2$	1.266	3.206	1.735	1.000	2.000	3.500
$(\|E\|^2 - 1)^3$	2.557	19.302	4.864	2.000	8.000	26.000
$\|\|E\|^2 - 1\|^3$	3.177	20.300	5.587	2.415	8.691	26.903

systematic error leads to least-square Δ's which are unrelated to the random error $s(I)$. The final R value, based on all observations with a unit weight, had a value of 0.106.

It is impossible to eliminate the pseudo-symmetry present in the crystal structure. However, we enhanced the I-centring related problems by the select use of intensities during the structure optimization. The selection rule $I > 3\sigma\ (I)$ favours the use of data with $(h + k + l) = 2n$. We decided to remedy the shortcomings produced by this selection mechanism by background modelling.

A reinterpretation of the original Mach3 data was made using the background model $B(\theta)$. The application of the background model does not repair the systematic intensity errors caused by a scan-angle-induced signal truncation. 223 observations were eliminated because they were systematically extinct. The modelling operation allowed us to refine the CuHM structure using the remaining 4117 observations. This had practically no impact on the geometry. The influence on B_{eq} values is limited as we can see in Tables 3(*a*) (FA model) and 4 (LO and HO model). The increase in the number of observations leads to an increased wR value (weights I^{-1}) of 0.065. The reduction in random error triggers an increase in S. Its value changes from 3.15 (BPB) to 4.11. The behaviour of the unweighted R is encouraging. Its BPB value of 0.106 reduces to 0.084, as the consequence of the introduction of the background model. The improvement is in our opinion logical, because the replacement of the observation $B(\vec{H})$ by its posterior value $\langle b|B\rangle$ rectifies the 'hit and run' quality of $B(\vec{H})$.

$B(\theta)$ was calculated from intensity measurements made after the preliminary scan. Those data are not biased by the applied measuring strategy. Replacing B(preliminary scan) by $\langle b|B\rangle$ one eliminates the strategy-induced background bias completely.

The BPB data set and the background model inferred data set produce practically identical geometries. The maximum shift of 0.003 Å was observed in the bond length C2—C3. This change is equal to a single e.s.d. and is thus insignificant. In the atomic displacements we observed a small shift in $B_{eq}(Cu^{2+})$. Its value goes from 1.585 (4) to 1.597 (4) Å^2; this shift of three e.s.d.'s is in our opinion not significant. All other B_{eq} values change less than 3 e.s.d.'s.

Atom O1 is again a remarkable exception. Its B_{eq} value changes from 3.09 (3) to 2.82 (3) Å^2 in the FA refinement. This shift of 9 e.s.d.'s is significant. We prefer the latter value, obtained from net intensities calculated *via* the background model. Our preference is based on the intuitively expected equivalence between B(O1) and B(O3).

The proposed reconstruction of net intensities will always result in positive intensity estimates. This is true even when the observed raw intensities become practically equal to the background. Therefore, in order to use the reconstruction we checked the original data for signs indicative of non-zero reflection intensities. The difference between $\langle B\rangle_\theta$ and $\langle R\rangle_\theta$ is a useful discriminator. At high θ values it is not very efficient, because $\langle B\rangle$ and $\langle R\rangle$ become practically equal. Higher moments of the samples $\{B\}_\theta$ and $\{R\}_\theta$ are more usefull. The skewness is a promising criterion. Up to 45° in θ we found a positive skewness for $P(R)$, *i.e.* $P(R)$ tails in the direction of high intensities. The skewness of $P(B)$ is zero and thus $P(B)$ is symmetric. Those two distribution skewnesses, calculated per θ interval, allowed us to decide that the intensity reconstruction could be applied sensibly.

6. Discussion of the structure

Bond distances and valence angles are summarized in Table 6. In the Cu complex the metal coordination clearly shows the geometrical pattern typical for the Jahn–Teller effect. The equatorial bonds between manganese(II) and the hydrogen malonate moiety are ∼0.1 Å longer than those in the copper(II) derivative. The axial M—OW distance shows the reverse with Cu—OW about 0.3 Å longer than Mn—OW. In the MgHM salt (Briggman & Oskarsson, 1978) an analogous metal coordination exists. In the absence of complexation all Mg—O distances are almost the same at 2.05 Å.

As pointed out by *e.g.* Kalsbeek (1992) the C—C distances to an ionized and an unionized carboxyl group in the acid salt of a dicarboxylic acid are in general different. In the Mg salt (Briggman & Oskarsson, 1978) the C—C distances are 1.503 (1) and 1.523 (1) Å for the acid and the ionized group, respectively. Similar values of 1.503 (1) and 1.539 (1) Å are observed in NaHM (Kalsbeek, 1992). In the CsHM salt (Soriano-Garcia *et al.*, 1988) the reported values are roughly the same, *viz* 1.500 (8) and 1.507 (7) Å. The C—C distances in CuHM and MnHM are practically identical.

When we compare the hydrogen malonate geometries in the Cu and Mn structures we observe a significant shift of 0.017 Å (6 e.s.d.'s) in the bond distance C3—O3. In both structures O3 acts twice as an acceptor in the hydrogen bonds formed with two different water molecules (see Table 6*b*). The angle OW^{i}—O3—OW^{ii} is 110.15 (3)° in CuHM and increases to 112.60 (2)° in MnHM. In the latter structure the donor–acceptor distances are shorter. Stronger hydrogen bonds help to elongate C3—O3.

In our structures the hydrogen malonate ions are almost planar. In CuHM the torsional angles O1—C1—C2—C3 and

Table 6
Interatomic distances (Å) and valence angles (°).

	Cu			Mn
	Mach3 294 K	CAD-4 294 K	CAD-4 120 K	CAD-4 294 K
M—O2	1.968 (1)	1.963 (2)	1.972 (1)	2.042 (2)
M—O4	1.935 (1)	1.933 (2)	1.936 (1)	2.033 (1)
M—O*w*	2.479 (2)	2.477 (2)	2.427 (1)	2.187 (2)
O2—*M*—O4	93.45 (5)	93.45 (8)	93.54 (5)	90.06 (7)
O2—*M*—O*w*	86.27 (5)	86.26 (8)	85.62 (5)	86.93 (7)
O4—*M*—O*w*	91.03 (5)	90.89 (8)	90.74 (5)	91.13 (6)
O1—C1	1.324 (2)	1.383 (6)	1.325 (2)	1.326 (3)
O2—C1	1.250 (2)	1.254 (3)	1.251 (2)	1.250 (3)
C1—C2	1.499 (2)	1.489 (4)	1.506 (2)	1.505 (3)
C2—C3	1.502 (3)	1.514 (6)	1.509 (2)	1.508 (3)
C3—O3	1.244 (2)	1.242 (3)	1.250 (2)	1.261 (3)
C3—O4	1.269 (2)	1.260 (4)	1.267 (2)	1.259 (3)
O1—H11	1.09 (3)	1.07 (3)	0.99 (1)	1.27 (1)
O*w*—H1*w*	0.70 (2)	0.67 (4)	0.85 (1)	1.04 (2)
O*w*—H2*w*	0.80 (3)	0.70 (4)	0.74 (1)	0.93 (1)
C2—H21	0.82 (3)	0.53 (6)	0.97 (3)	0.98 (3)
C2—H22	1.12 (4)	0.96 (7)	1.05 (3)	1.00 (4)
O1—C1—O2	120.9 (2)	120.6 (2)	120.9 (1)	120.5 (2)
O1—C1—C2	114.3 (1)	114.4 (2)	114.3 (1)	114.7 (2)
O2—C1—C2	124.8 (2)	125.0 (2)	124.8 (2)	124.8 (2)
C1—C2—C3	122.1 (2)	122.0 (2)	121.8 (1)	122.5 (2)
C2—C3—O3	115.3 (1)	114.8 (3)	114.9 (1)	114.8 (2)
C2—C3—O4	122.6 (1)	122.3 (3	122.9 (1)	122.9 (2)
O3—C3—O4	122.2 (2)	123.0 (4)	122.2 (2)	122.3 (2)

(*b*) Hydrogen bonds

	Cu Mach3 294 K	Cu CAD-4 120 K	Mn CAD-4 294 K
O3···Ow^{i}	2.721 (2)	2.705 (2)	2.712 (2)
O3···Ow^{ii}	2.753 (2)	2.731 (2)	2.731 (3)
O3···H1w^{i}	2.03 (2)	1.89 (3)	1.76 (6)
O3···H2w^{ii}	1.92 (3)	1.97 (3)	1.80 (3)
∠O3···H1*w*—Ow^{i}	169 (2)	168 (3)	153 (4)
∠O3···H2*w*—Ow^{ii}	171 (2)	166 (3)	167 (4)
Ow^{iii}···O1	2.865 (2)	2.846 (2)	2.989 (2)
Ow^{iii}···Hh	1.91 (2)	1.78 (4)	
∠Ow^{iii}—H1*w*···O1	177 (1)	164 (3)	

Symmetry codes: (i) $\frac{3}{2}-x,-\frac{1}{2}+y,\frac{3}{2}-z$; (ii) $-1+x,y,z$; (iii) $\frac{3}{2}-x,\frac{1}{2}+y,\frac{3}{2}-z$.

O3—C3—C2—C1 are −179.0 (1) and 172.3 (2)°, respectively. Almost planar hydrogen malonate moieties have also been observed in the MgHM salt. Here the unionized carboxyl group forms a short hydrogen bond of 2.59 Å with an adjacent HM moiety. This packing scheme is absent in the present structures.

H11 is in our structure model the H atom of the unionized carboxyl group. This choice is not necessarily the correct one. In all structure determinations the difference electron density map suggests an alternative position Hh. Its peak height in e Å^{-3} is less than the maximum for H11. Both H11 and Hh are located in the molecular plane with torsional angles of 176 (3) and −4 (3)° for C2—C1—O1—H11 and C2—C1—O1—Hh, respectively. The position of Hh can be refined and converges to [0.607 (6), 0.545 (5), 0.873 (4)] in CuHM. Its final *B* value is significantly larger than B(H11). A combined refinement with H11 and Hh is also possible. However, when we assign an occupancy of 0.5 to both positions, we obtain negative *B* values for both H11 and Hh. A simple criterion such as the lowest *R* value led to H11. In terms of intermolecular interactions Hh has to be preferred. Hh allows O1 to act as a proton donor towards OW^{iii}.

7. Analysis of CuHM at 120 K

In §5 we reduced the problems of the pseudo-*I*-centring by increasing the number of observations included in the least-squares analysis using background modelling. In our view the background subtraction using the background polynomial produced the best possible set of data at a given temperature. The decrease in the detection limit – here linked to $\sigma(I)$ – is responsible for the increase in the number of 'observed' data. Preserving the traditional BPB procedure in the calculation of $I_{\rm net}$ and $\sigma^2(I)$ it is possible to increase the number of observations by lowering the temperature. We decided to do so in order to find parallels between the model response and the increased size of the data set.

We redetermined the CuHM structure at 120 K on our CAD-4 equipment. The crystal was cooled by a N_2 flow from an Enraf–Nonius FR 558-NH cryostat. All symmetry-independent reflections were measured up to 45° in θ. In the BPB analysis this resulted in 2972 data with $I > 3\sigma$. Details of the analysis are given in Table 2.

For an harmonic oscillator the *B* values ($B = 8\pi^2 U$) decrease linearly with *T*. Thus, the $B_{\rm eq}$ values at 120 K are expected to be $0.41 \times B$ (294 K). The final values for $B_{\rm eq}$ (120 K) are listed in Table 3(*c*). Their values are roughly in line with those observed at room temperature (Table 3*a*). This is also true for $B_{\rm eq}$ (C_2). Therefore, its exceptionally large value cannot be linked to a double well potential generating *e.g.* static disorder at low temperature.

The reduction in temperature allowed us to increase the number of significant observations ($I > 3\sigma$) from 1910 to 2972. As shown in Table 3(*c*) $B_{\rm eq}$ (O1) has a value of 1.37 (2) Å^2. For O3 we find a *B* value of 1.16 (2) Å^2. Compared to the room-temperature measurement the difference between *B*(O1) and *B*(O3) is smaller at 120 K. This is in line with our intuitive expectation based on the symmetry in the Cu complex. As such, the temperature-induced increase in the number of observed reflections has the same effect on *B*(O1) and *B*(O3) as the increase in number of observations produced by the alternative background analysis routine at room temperature.

Finally, we looked into the unsolved ambiguity between the atoms H11 and Hh. The low-temperature data produced the same result as observed in the room-temperature analysis. The structure model, which included H11, gives the best fit with the data ($wR = 0.053$ and $uR = 0.048$). The replacement of H11 by Hh increases the residual values to 0.055 and 0.049 for *wR* and *uR*, respectively.

8. Conclusions

Reproducibility is an important issue in a structure determination. With our standard laboratory equipment (CAD-4/stationary anode) we have found that the B(model) overestimates the real atomic displacements B(true). A graphite-monochromated Mo beam, generated with a tube voltage of 50 kV, leads roughly to: $B(\text{model}) \simeq B(\text{true}) + 0.1$ Å^2 (see Rousseau *et al.*, 2000). The discrepancy between B(model) and B(true) is caused by intensity profile truncation errors, which are produced by the mismatch between the applied scan angle and the wavelength dispersion in the monochromated X-ray beam. For intensities in the range $0 < \theta < 30^\circ$ the average truncation error is ~3%. For intensities with $30 < \theta < 45^\circ$ the average error is about 10%. This difference in truncation error explains in our view the discrepancy between the scale factors calculated with HO and LO data, respectively.

The intensity truncation error in the Mach3 data was increased by the misfit between the detector aperture and the mosaicity of the crystal looked at. We find B(Mach3) = B(CAD-4) + 0.1 Å^2. The intensity truncation by the aperture influences B_{eq} values. Again the systematic intensity error is easily randomized. Fortunately, the S values clearly point towards a difference between the least-square Δ's and the random σ's.

These conclusions were obtained while working with selected sets of data ($I > 3\sigma$). Background modelling made it possible to refine our structure using all observations. The immediate reduction in the R value, calculated with all reflections, from 10.6 to 8.4% reveals that the background modelling procedure is a significant step in the proper direction. It does not alter the above-mentioned consequences of the systematic intensity errors made during data collection.

When an $\omega/2\theta$ scan mode is applied during data collection, the scan angle induced spectral truncation error is visible twice, *viz*. (i) one underestimates the raw intensity R and (ii) one overestimates the local background B. We ignored this latter aspect in our analysis leading towards the background polynomial. The zero-skewness in $P(B)$ (see previous section) does not contradict this practical approach. The impact of the signal overflow on $\langle B \rangle_\theta$ is in general small compared with the counting statistical variance $\sigma^2(B)$. For the strongest reflections, however, this is not true. For these reflections we find – in retrospect – that B(observed) is incompatible with the expected background b, *i.e.* $P(B|b) = 0$. In such circumstances we calculated I_{net} using the BPB procedure rather than the background model. Since B is negligible compared to R, we again have a situation with $\sigma^2(I_{net}) \simeq I_{net}$.

The Bayesian procedure used to prevent negative intensities produces posterior values for I_{net}. We used a uniform prior $P(i)$ for $i \geq 0$. This approach has a disadvantage, because it treats our observations in a θ-independent fashion. Nevertheless, the mean intensity Σf^2 decreases with θ. At high θ values ($s \simeq 0.9$ Å^{-1}) the current reconstruction produces a minimum $|F_{obs}|$ value of ~1 electron. This value is too large compared with the structure model inferred $|F_{calc}|$ values. Therefore, we intend to replace the uniform distribution $P(i)$ by the more appropriate Wilson distributions for $P1$ or $P\bar{1}$. This has been proposed by French & Wilson (1978) and Blessing (1987).

References

Blessing, R. H. (1987). *Cryst. Rev.* **1**, 3–58.
Bommel, A. J. van & Bijvoet, J. (1958). *Acta Cryst.* **11**, 61–70.
Briggman, B. & Oskarsson, Å. (1978). *Acta Cryst.* B**34**, 3357–3359.
Eisenstein, M. & Hirshfeld, F. L. (1983). *Acta Cryst.* B**39**, 61–75.
Enraf–Nonius (1994). *CAD4-Express Operations Manual.* Delft, The Netherlands.
Fair, C. K. (1990). *MolEN User's Manual.* Enraf–Nonius, Delft, The Netherlands.
French, S. & Wilson, K. (1978). *Acta Cryst.* A**34**, 517–525.
Hirshfeld, F. L. & Rabinovich, D. (1973). *Acta Cryst.* A**29**, 510–513.
Kalsbeek, N. (1992). *Acta Cryst.* C**48**, 878–883.
Lenstra, A. T. H., Bracke, B., van Dijk, B., Maes, S. T., Vanhulle, C. & Desseyn, H. O. (1998). *Acta Cryst.* B**54**, 851–858.
Lenstra, A. T. H., Geise, H. J. & Vanhouteghem, F. (1991). *Acta Cryst.* A**47**, 597–604.
Lenstra, A. T. H., Verbruggen, M., Bracke, B., Vanhouteghem, F., Reyniers, F. & Borremans, F. (1991). *Acta Cryst.* B**47**, 92–97.
Lenstra, A. T. H. & Rousseau, B. (1999). *Acta Cryst.* A**55** Supplement, Abstract P09.13.019.
Maes, S. T. (1997). Ph.D. Thesis. University of Antwerp (UIA), Belgium.
Maes, S. T., Vanhulle, C. & Lenstra, A. T. H. (1998). *Acta Cryst.* A**54**, 399–410.
North, A. C. T., Phillips, D. C. & Mathews, F. S. (1968). *Acta Cryst.* A**24**, 351–359.
Rousseau, B., Maes, S. T. & Lenstra, A. T. H. (2000). *Acta Cryst.* A**56**, 300–307.
Soriano-Garcia, M., Toscano, R., Villena, R., Rodriguez, A. & Campero-Celis, A. (1988). *J. Crystallogr. Spectrosc. Res.* **18**, 671–678.